

Computer Programs in Physics

QPC-TDSE: A parallel TDSE solver for atoms and small molecules in strong lasers [☆]Zhao-Han Zhang ^{a,*}, Yang Li ^a, Yi-Jia Mao ^a, Feng He ^{a,b}^a Key Laboratory for Laser Plasmas (Ministry of Education) and School of Physics and Astronomy, Collaborative Innovation Center for IFSA (CICIFSA), Shanghai Jiao Tong University, Shanghai 200240, China^b CAS Center for Excellence in Ultra-intense Laser Science, Shanghai 201800, China

ARTICLE INFO

Article history:

Received 5 February 2023

Received in revised form 23 March 2023

Accepted 15 May 2023

Available online 23 May 2023

Keywords:

Time-dependent Schrödinger equation

B-spline functions

Photo-electron momentum distribution

High harmonic generation

ABSTRACT

The QPC-TDSE program serves as a general tool to study laser-driven dynamics of electrons in ideal isolated atoms and molecules by solving the full-dimensional non-relativistic time-dependent Schrödinger equation (TDSE) within single-active-electron approximation. It expands the full-dimensional electronic wavefunction in spherical coordinates by spherical harmonics and B-spline functions and employs a set of parallel Crank-Nicolson propagators combined with split-operator techniques to evolve the wavefunction in time, which support centrifugal and multi-polar static potentials to treat atomic and molecular scenarios and accepts arbitrary combinations of linearly or elliptically polarized lasers within the dipole approximation. The program is capable of extracting the photo-electron momentum distribution via t-SURFF approach or projection onto either the exact scattering states or the planewaves. Its applications in different scenarios are given as examples, e.g., above threshold ionization, attosecond clock, higher-order harmonic generation.

Program summary

Program Title: QPC-TDSE

CPC Library link to program files: <https://doi.org/10.17632/xjm3kfgv75.1>

Licensing provisions: GPLv3

Programming language: C++

External libraries: HDF5, GSL, MKL

Nature of problem: Numerical solution of TDSE and extraction of various types of electron spectrum.

Solution method: The electronic wavefunction is expanded by B-spline functions and spherical harmonics whose range is chosen elaborately to reduce the total number of partial waves for non-linearly polarized lasers. The Crank-Nicolson approach combined with an operator-splitting scheme is used to propagate the wavefunction in time, either in velocity gauge or length gauge. Matrix inversions are solved via either dense or sparse linear algebra solvers according to their structures. The t-SURFF method and projections onto either the scattering states or planewaves are provided for the accurate extraction of the momentum distributions.

Additional comments including restrictions and unusual features: Only lasers within dipole approximation are supported. For the multi-polar potentials, only pure Coulombic ones are supported. Routines for solving exact scattering states have only been implemented for centrifugal potentials. The codes are written in C++17 and can only be compiled on the platforms that support the avx instruction sets. An extension for the propagation algorithm using the avx-512 intrinsics is provided as optional.

© 2023 Elsevier B.V. All rights reserved.

[☆] The review of this paper was arranged by Prof. W. Jong.

* Corresponding author.

E-mail address: zhangzhaohan@sjtu.edu.cn (Z.-H. Zhang).

1. Introduction

Ionization and excitation dynamics of isolated atoms and molecules driven by intense lasers are extremely interested in attosecond physics [1]. To understand them, various physical quantities are measured or computed to assist their analysis, including the photo-electron momentum distribution (PMD) [2], high-order harmonic spectra (HHS) [3], attosecond transient absorption spectra (ATAS) [4], etc. A large variety of theoretical approaches to extract them are established upon the direct numerical solution of the time-dependent Schrödinger equation (TDSE), which in principle describes the electronic dynamics faithfully in a comprehensive quantum manner. However, as the computational resources required by solving TDSE grow exponentially with respect to the degree of freedom, most discussions of full-dimensional systems are restricted to the single-active-electron (SAE) approximations. Solving the full two-active-electron TDSE is still a computationally heavy problem for multi-photon processes [5], while a direct treatment of more than two active electrons without further approximations, such as the multi-configurational time-dependent Hartree (MCTDH) theory [6] and the time-dependent density functional theory (TDDFT) [7], is still absent from the literature. Even within SAE, an accurate solution under extreme conditions is still challenging. Various open source programs and softwares have been developed to solve TDSE efficiently. QPROP [8] propagates the SAE or DFT wavefunction expanded by spherical harmonics and uniform finite difference grids with an exquisite operator-splitting scheme, which achieves a linearly scaling computational complexity concerning the expansion size. Although its propagation algorithm is parallelizable, it has not been implemented yet. CLTDSE [9] also expands the SAE wavefunction in spherical coordinates for only linearly polarized cases but parallelizes the propagation by GPU. SCID-TDSE [10] resolves the propagation in a reference frame rotating with the direction of laser polarization to block-diagonalize most of the Hamiltonian matrices and reduce the total number of partial waves in the expansion for non-linearly polarized lasers. It also extends the finite difference grid to a non-uniform one. ALTDSE [11] adopts a flexible parallel Lanczos-Arnoldi solver which accounts for multi-electronic effects by preparing the accurate dipole matrix and field-free Hamiltonian matrix. PCTDSE [12] parallelly solves TDSE on a general uniform finite difference Cartesian grid by a split-operator method combined with fast Fourier transforms. Such a grid is favorable for generalization but limits the accurate description of the target system near the Coulomb poles.

The current QPC-TDSE program replaces the radial finite difference grid with an expansion with B-spline functions [13] to reduce the sizes of radial arrays and matrices without compromising on the numerical accuracy. For the spherical harmonics, a special expansion scheme other than a full expansion is designed to overcome the difficulties arising from the uncontrollably large number of partial waves encountered for the strong lasers, especially the elliptically polarized ones. Projection onto the exact scattering states [14,15] and t-SURFF [16] are provided for the accurate acquisition of photo-electron momentum distributions. Besides, the current code also supports static molecular potentials implemented by the one-center expansions (OCE). Most functionalities are parallelized with OpenMP such that their efficient execution is available on shared memory processors.

The remaining part of this article is organized as follows. In Sec. 2, we sketch the fundamental theories behind the programs. In Sec. 3, the detailed implementations of the various numerical approaches in QPC-TDSE are introduced briefly. In Sec. 4, we give example runs for illustration. In Sec. 5, the limitations and possible extensions of the current programme are discussed.

2. Theory

2.1. Time-dependent Schrödinger equation

The non-relativistic dynamic of an electron exposed to a strong laser can be completely described by its wavefunction $\psi(\mathbf{r}, t)$. For such an electron interacting with classical (i.e. not quantized) external electromagnetic fields $V(\mathbf{r}, t)$ and $\mathbf{A}(\mathbf{r}, t)$, its time-evolution is governed by the time-dependent Schrödinger equation (atomic units $\hbar = e = m_e = 4\pi\epsilon_0 = 1$ are used throughout this paper)

$$i \frac{\partial \psi}{\partial t} = H \psi. \quad (1)$$

For the electron initially trapped in an atom or small molecule, the wavelength of the external laser field is typically far larger than the distance that the electron could reach during the whole period of the interaction, which enables the frequently adopted dipole approximation [17]. Within such approximation, the velocity gauge Hamiltonian reads

$$H = -\frac{1}{2} \Delta - i \mathbf{A}(t) \cdot \nabla + V(\mathbf{r}), \quad (2)$$

where $V(\mathbf{r})$ is the atomic or fixed-body molecular potential and $\mathbf{A}(t)$ is the vector potential of the dipolar field, which is associated with the electric field by $\mathbf{E}(t) = -\partial \mathbf{A}(t) / \partial t$. Another formally equivalent choice is the length gauge Hamiltonian

$$H = -\frac{1}{2} \Delta + \mathbf{E}(t) \cdot \mathbf{r} + V(\mathbf{r}). \quad (3)$$

Although both two gauges are supported in QPC-TDSE, we strongly recommend to choose velocity gauge whenever it is acceptable for its property of faster convergence in the expansion of spherical harmonics [18].

2.2. Photo-electron momentum distribution

As a consequence of photodetachment, the electron escapes from the ionic or neutral core and will reach infinity. If measured by detectors at infinity, its momentum distribution is rigidly expressed as [14]

$$P(\mathbf{k}) = |\langle \psi_{\mathbf{k}}^- | \psi_{t_f} \rangle|^2 \quad (4)$$

where t_f is the time after which the time-dependent part of eq. (2) or eq. (3) can be considered as vanishing, and $\psi_{\mathbf{k}}^-$ is the scattering state acquiring asymptotic momentum \mathbf{k} at infinity with incoming boundary condition. For one electron problem, it is not too demanding to numerically solve $\psi_{\mathbf{k}}^-$ for systems with spherical symmetry on the powerful modern parallel computers, which validates the direct use of eq. (4). Its implementation in QPC-TDSE will be explained in Sec. 3.9.

As shown in ref. [14], the following approach may also yield $P(\mathbf{k})$ asymptotically:

$$|\langle \phi_{\mathbf{k}} | \Pi | \psi_t \rangle|^2 \xrightarrow{t \rightarrow +\infty} P(\mathbf{k}) \quad (5)$$

where Π is the projection operator which projects out all bound states of the field-free part of eq. (2), and $\phi_{\mathbf{k}}$ is the plane wave with momentum \mathbf{k} . This validates the approximation

$$P(\mathbf{k}) \approx |\langle \phi_{\mathbf{k}} | \Theta_{r_0} | \psi_t \rangle|^2 \quad (6)$$

for sufficient large t and appropriate r_0 such that the heaviside operator Θ_{r_0} effectively projects out all bound states. A notorious problem for the above approaches is that a very large simulation box should be adopted to retain all wavepackets inside it. The t-SURFF [16] method and its extension i-SURF [19] improve the efficiency of eq. (6) by replacing the volume integral by a surface flux integral over time, which significantly reduces the box size and shortens the simulation time for long duration lasers. The key principle is that

$$P(\mathbf{k}) \approx \int_{-\infty}^{+\infty} |\langle \phi_{\mathbf{k},t}^V | [H^V, \Theta_{r_0}] | \psi_t \rangle|^2 dt \quad (7)$$

where

$$H^V = -\frac{1}{2} \Delta - i\mathbf{A}(t) \cdot \nabla \quad (8)$$

and $\phi_{\mathbf{k},t}^V$ is its corresponding Volkov solution with momentum \mathbf{k} at t . Note that the commutator in eq. (7) is non-vanishing only on the surface $|\mathbf{r}| = r_0$. QPC-TDSE implements t-SURFF only for velocity gauge, which is to be discussed in Sec. 3.10.

2.3. High-order harmonic spectra and attosecond transient absorption spectra

Both high harmonic spectra and attosecond transient absorption spectra are obtainable from TDSE results via dipole moment or dipole acceleration of the electron. For HHS, the power of the generated radiation of an isolated atomic or molecular target is [20]

$$S_i(\omega) = \frac{4\pi^2\omega^2}{c^2} |\tilde{d}_i(\omega)|^2 \times 2\pi, \quad (9)$$

where $c \approx 137.036$ is the speed of light. For ATAS, the absorption spectra are given by [21]

$$S_i(\omega) = 2\text{Im}[\tilde{d}_i(\omega)\tilde{E}_i^*(\omega)]. \quad (10)$$

Note the label $i = x, y, z$ indicates the direction, and a quantity with a tilde indicates a Fourier transform, e.g.

$$\tilde{d}_i(\omega) = \frac{1}{\sqrt{2\pi}} \int_{-\infty}^{+\infty} d_i(t) \exp(i\omega t) dt. \quad (11)$$

The extra 2π factor in eq. (9) originates from the different definition in the factor of Fourier transform.

In QPC-TDSE, either dipole moment or dipole acceleration can be optionally recorded during propagation for subsequent evaluation of the above spectrum.

3. Implementation

3.1. Potentials

QPC-TDSE accepts potentials in the form $V(\mathbf{r}) = V_c(r) + U(\mathbf{r})$, where $V_c(r)$ is an arbitrary close-form function of r and

$$U(\mathbf{r}) = - \sum_{\nu=0}^{N_{\text{pole}}-1} \frac{Z_{\nu}}{|\mathbf{r} - \mathbf{R}_{\nu}|}. \quad (12)$$

The latter is a special case of the general multi-polar potential

$$U(\mathbf{r}) = \sum_{\mu\lambda} \left\{ \sum_{\nu} C_{\lambda\mu}^{\nu} V_{\lambda\mu}^{\nu}(r) \right\} Y_{\lambda}^{\mu}(\theta, \varphi). \quad (13)$$

By matching to the one-center multi-polar expansion of eq. (12), the essential quantities in eq. (13) are uniquely determined by $\mathbf{R}_{\nu} = (R_{\nu}, \Theta_{\nu}, \Phi_{\nu})$ and Z_{ν} , i.e.

$$C_{\mu\lambda}^v = -\frac{4\pi Z_v}{2\lambda + 1} Y_{\lambda}^{\mu*}(\Theta_v, \Phi_v), V_{\mu\lambda}^v(r) = \frac{[\min(r, R_v)]^\lambda}{[\max(r, R_v)]^{\lambda+1}}. \quad (14)$$

The range of the summation over $\mu\lambda$ will be specified later. To avoid repetitive evaluation of the potential $V_{\mu\lambda}^v$ in eq. (14), repetitive R_v -s should be given only once. As a consequence, to enable and initialize the multi-polar potential $U(\mathbf{r})$, users should set the parameter vector $\{R_v, (Z_{v,0}, \Theta_{v,0}, \Phi_{v,0}), (Z_{v,1}, \Theta_{v,1}, \Phi_{v,1}), \dots, (Z_{v,n_{\text{pole}}-1}, \Theta_{v,n_{\text{pole}}-1}, \Phi_{v,n_{\text{pole}}-1})\}$. For example, for HeH^{2+} aligned in z-direction, users may set $V_c(r) = 0$, $R_0 = R/2$, $(Z_{0,0} = 2, \Theta_{0,0} = 0, \Phi_{0,0} = 0)$, $(Z_{0,1} = 1, \Theta_{0,1} = \pi, \Phi_{0,1} = 0)$ with R the internuclear distance.

3.2. Laser fields

The current propagation algorithm in QPC-TDSE is designed for dipole fields. It relies on the values of the fields at discrete sample points $\{t_j\}_{j=0}^{N_t}$ to work, i.e. $A_x(t_j)$, $A_y(t_j)$, $A_z(t_j)$ or $E_x(t_j)$, $E_y(t_j)$, $E_z(t_j)$. To reduce the number of the factorized matrices which we will introduce in the subsequent sections, we use a uniformly distributed time points $t_j = t_0 + j\Delta t$. Fields in QPC-TDSE are supposed to be a summation of several independent parts:

$$F_s(t_j) = \sum_{i=0}^{N_s-1} F_{si}(t_j), \quad (15)$$

where $s = x, y, z$, and the function F_{si} is to be specified by the user. Here F_s is interpreted as $A_s(E_s)$ for velocity (length) gauge and is switched off when the corresponding N_s is set to zero. Although such implementation covers most of the common situations in researches, there could still be exceptions. However, the extension to the original code is not difficult, for details please look up the user guide.

3.3. Wavefunction

The wavefunction to be propagated is expanded via

$$\psi(\mathbf{r}t) = \frac{1}{r} \sum_{nlm} c_{nlm}(t) B_n(r) Y_l^m(\theta, \varphi), \quad (16)$$

where $Y_l^m(\theta, \varphi)$ are spherical harmonics in standard definition in quantum mechanics, $B_n(r)$ are a set of B-spline functions in the same order M and defined on a given knot sequence. For the current code, the first and last B-spline functions are removed to impose zero boundary conditions on both sides. If the multi-polar potential is enabled, the positions of some of the knots are automatically enforced to satisfy the cusp condition at Coulomb poles [13]. In our context, the user-given $\{R_v\}_{v=0}^{N_v-1}$ will be used as intermediate knots and repeated for $M - 1$ times to impose discontinuous derivatives of the wavefunction at these points. For all partial waves included in the computation, the same set of B-spline functions are used. The current implementation uses linearly-spaced knot sequence inside each interval isolated by the poles, and assign values to them automatically according to the user-given parameters $r_{\min} = 0$, $R_0, R_1 \dots R_{N_v-1}, r_{\max}$ and $K_0, K_1 \dots K_{N_v-1}$. Their detailed description is found in the manual.

The range of summation in eq. (3.3) indeed needs serious considerations. Conventionally, a full expansion including all possible (l, m) until $l = l_{\max}$ is used for the general cases, which is also the choice of ref. [8]. For the special cases that the Hamiltonian of the laser-driven system is invariant under the rotation around a fixed axis, which could happen for example when the laser is linearly polarized, one may only choose the partial waves with the same m to the initial state to reduce the computational costs. QPC-TDSE adopts a flexible expansion scheme to cover the above cases. We conceptually map the label (n, l, m) to a non-negative integer vector (i_n, i_l, i_m) whose ranges are given by $i_n < N_r$, $i_l < N_l$, $i_m < N_m$, using the following transform:

$$m = m_0 + i_m, l = |m_0 + i_m| + i_l, n = i_n \quad (17)$$

where m_0 is a user-given integer to designate the lowest value of m occurred in eq. (16). To map (i_n, i_l, i_m) onto a contiguous memory, we use $i = i_m N_l N_r + i_l N_r + i_n$ thus a total size of $N_r N_l N_m$ is required for the storage of c_{nlm} . See Fig. 1 for a comparative example about the indexing scheme for the angular basis when $m_0 = -2$, $N_l = 4$, $N_m = 5$. The advantage of this scheme is to be discussed in later sections.

The exact values of N_m, N_l, N_r for the propagation to converge, however, vary from case to case and should be carefully tested. For example, the maximal electron momentum p_{\max} that can be accurately described by the basis is controlled by the value of N_r and r_{\max} . Empirically one may use the relation $p_{\max} \approx \beta \pi N_r / r_{\max}$ to estimate the proper value of N_r , where β is usually a value between 0.5 to 1.0. Satisfactory results were obtained using $N_{\max} / r_{\max} \approx 2.0$ for all the examples provided in the later sections in this article, however, it is not necessary a universal law to be so. For example, in ref. [22], convergency of the ionization yields of an hydrogen atom can be reached using $N_{\max} / r_{\max} \approx 1.0$.

3.4. Matrix element

By imposing Galerkin condition with eq. (16), eq. (1) is transformed into a group of linear ordinary differential equations, which reads in matrix form

$$iSc(t) = [\mathcal{T} + \mathcal{U} + \mathcal{W}^+(t) + \mathcal{W}^-(t) + \mathcal{W}^z(t)]c(t). \quad (18)$$

Here, S is the overlap matrix arising from the non-orthogonality of B-spline functions; \mathcal{T} is the matrix of kinetic operator together with the centrifugal potential V_c ; \mathcal{U} is the matrix of the non-centrifugal potential U ; $\mathcal{W}^z, \mathcal{W}^\pm$ are the dipole interaction matrix triggered by $F_z, F_\pm = [F_x \pm iF_y]/2$, respectively.

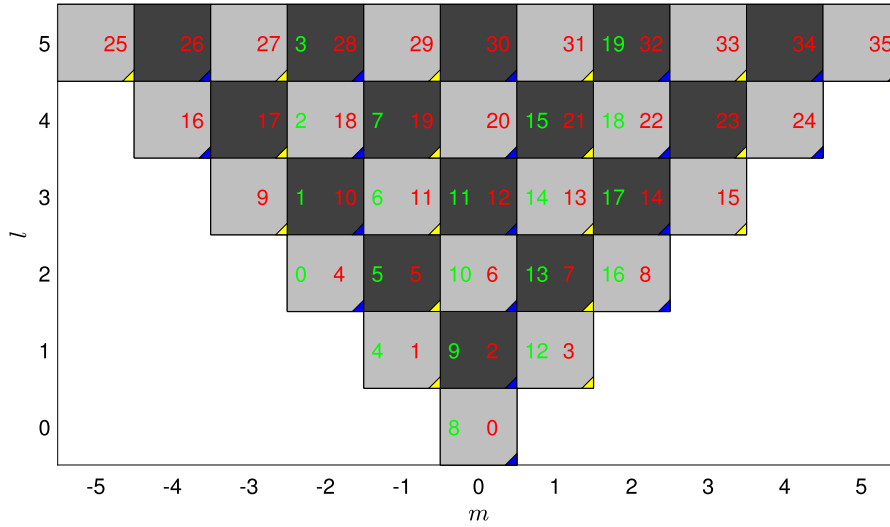


Fig. 1. An illustration of the expansion scheme. A non-blank block represents a partial wave labeled by (l, m) . Blocks with dark (light) shades have odd (even) values of $l - |m|$ and they are classified as odd (even) space. They are completely disconnected during the interaction with the lasers polarized inside the $x - y$ plane if only dipolar transitions are considered. Besides, linearly polarized lasers in z direction conserve m and only induce transitions between the blocks whose corners are painted in the same color. The index in a full expansion given by $(l+1)l+m$ is indicated by red integers, while the index scheme used in QPC-TDSE is indicated by green ones. (For interpretation of the colors in the figure(s), the reader is referred to the web version of this article.)

The row and column index of these matrices, i and j , are just the 1D-index mentioned in the previous section, and their corresponding value vector is denoted by (n_i, l_i, m_i) and (n_j, l_j, m_j) , respectively. Using such convention, we may list the matrix elements in a contracted way. The overlap matrix, centrifugal Hamiltonian matrix, non-centrifugal potential matrix and dipole interactions in velocity and length gauges are

$$S_{ij} = \delta_{m_i m_j} \delta_{l_i l_j} S_{n_i n_j}, \quad (19)$$

$$T_{ij} = \delta_{m_i m_j} \delta_{l_i l_j} T_{n_i n_j}^{l_i}, \quad (20)$$

$$U_{ij} = \sum_{\lambda, \mu} A_{m_i m_j, l_i l_j}^{\lambda, \mu} U_{n_i n_j}^{\lambda, \mu}, \quad (21)$$

$$\mathcal{W}_{ij}^s(t) = -A_s(t) \left(P_{m_i m_j, l_i l_j}^s D_{n_i n_j} + Q_{m_i m_j, l_i l_j}^s L_{n_i n_j} \right), \quad (22)$$

$$\mathcal{W}_{ij}^s(t) = E_s(t) P_{m_i m_j, l_i l_j}^s R_{n_i n_j}. \quad (23)$$

The radial integrals occurred in eqs. (19), (20), (21), (22), (23) are

$$S_{n_i n_j} = \int_{r_i}^{r_f} B_{n_i}(r) B_{n_j}(r) dr, \quad (24)$$

$$T_{n_i n_j}^{l_i} = \int_{r_i}^{r_f} B_{n_i}(r) \left(-\frac{1}{2} \frac{d^2}{dr^2} + \frac{l_i(l_i+1)}{2r^2} + V_c(r) \right) B_{n_j}(r) dr, \quad (25)$$

$$U_{n_i n_j}^{\lambda, \mu} = \int_{r_i}^{r_f} B_{n_i}(r) \left(\sum_{\nu} C_{\lambda, \mu}^{\nu} V_{\lambda, \mu}^{\nu}(r) \right) B_{n_j}(r) dr, \quad (26)$$

$$D_{n_i n_j} = i \int_{r_i}^{r_f} B_{n_i}(r) \frac{d}{dr} B_{n_j}(r) dr, \quad (27)$$

$$L_{n_i n_j} = \int_{r_i}^{r_f} B_{n_i}(r) \frac{1}{r} B_{n_j}(r) dr. \quad (28)$$

$$R_{n_i n_j} = \int_{r_i}^{r_f} B_{n_i}(r) r B_{n_j}(r) dr. \quad (29)$$

All of the radial integrals are in symmetric or Hermitian band structure due to the local support of B-spline functions. They are thus stored in standard LAPACK layout, each occupies an array of size $(M+1)N_r$. Their evaluations are separately performed via Gauss-Legendre quadratures on each interval where the B-splines are piecewisely defined. The quadrature order is empirically chosen as $2M+2$. Quadrature points and weights are provided by GSL. The value of B-spline functions on Gauss points is computed by definition.

Angular integrals are performed analytically,

$$P_{m_i m_j, l_i l_j}^z = \delta_{m_i m_j} \delta_{l_i l_j - 1} \sqrt{\frac{l_j^2 - m_i^2}{(2l_j - 1)(2l_j + 1)}} + \delta_{m_i m_j} \delta_{l_i l_j + 1} \sqrt{\frac{l_i^2 - m_i^2}{(2l_i - 1)(2l_i + 1)}} \quad (30)$$

$$P_{m_i m_j, l_i l_j}^+ = \delta_{m_i m_j - 1} \delta_{l_i l_j + 1} \sqrt{\frac{(l_i - m_i)(l_i - m_i - 1)}{(2l_i - 1)(2l_i + 1)}} - \delta_{m_i m_j - 1} \delta_{l_i l_j - 1} \sqrt{\frac{(l_j + m_j)(l_j + m_j - 1)}{(2l_j - 1)(2l_j + 1)}} \quad (31)$$

$$P_{m_i m_j, l_i l_j}^- = \delta_{m_i m_j + 1} \delta_{l_i l_j - 1} \sqrt{\frac{(l_j - m_j)(l_j - m_j - 1)}{(2l_j - 1)(2l_j + 1)}} - \delta_{m_i m_j + 1} \delta_{l_i l_j + 1} \sqrt{\frac{(l_i + m_i)(l_i + m_i - 1)}{(2l_i - 1)(2l_i + 1)}} \quad (32)$$

$$Q_{m_i m_j, l_i l_j}^z = i \delta_{m_i m_j} \delta_{l_i l_j - 1} \sqrt{\frac{l_j^2(l_j^2 - m_i^2)}{(2l_j - 1)(2l_j + 1)}} - i \delta_{m_i m_j} \delta_{l_i l_j + 1} \sqrt{\frac{l_i^2(l_i^2 - m_i^2)}{(2l_i - 1)(2l_i + 1)}} \quad (33)$$

$$Q_{m_i m_j, l_i l_j}^+ = i \delta_{m_i m_j - 1} \delta_{l_i l_j - 1} \sqrt{\frac{l_j^2(l_j + m_j)(l_j + m_j - 1)}{(2l_j - 1)(2l_j + 1)}} + i \delta_{m_i m_j - 1} \delta_{l_i l_j + 1} \sqrt{\frac{l_i^2(l_i - m_i)(l_i - m_i - 1)}{(2l_i - 1)(2l_i + 1)}} \quad (34)$$

$$Q_{m_i m_j, l_i l_j}^- = -i \delta_{m_i m_j + 1} \delta_{l_i l_j + 1} \sqrt{\frac{l_i^2(l_i + m_i)(l_i + m_i - 1)}{(2l_i + 1)(2l_i - 1)}} - i \delta_{m_i m_j + 1} \delta_{l_i l_j - 1} \sqrt{\frac{l_j^2(l_j - m_j)(l_j - m_j - 1)}{(2l_j + 1)(2l_j - 1)}} \quad (35)$$

The dipolar selection rules are implied in the Kronecker delta symbols. For the lasers elliptically polarized in the $x-y$ plane, $\Delta m = m_i - m_j = \pm 1$, $\Delta l = l_i - l_j = \pm 1$. One may find in Fig. 1 that the blocks in the same grayscale are connected by transitions invoked by such lasers, while the transitions between those blocks in different grayscales could never happen. The two separate subspaces are named even and odd spaces, referring to the fact that their values of $l-m$ are even or odd, respectively. For the linearly polarized lasers along the z axis, the selection rule reads $\Delta m = 0$, $\Delta l = \pm 1$. Therefore in Fig. 1, the blocks with corners painted in the same color are connected, while the transitions between those in different colors are forbidden.

For the multi-polar potential, the angular integral is

$$A_{m_i m_j, l_i l_j}^{\lambda \mu} = (-)^{m_i} \sqrt{\frac{(2l_i + 1)(2\lambda + 1)(2l_j + 1)}{4\pi}} \begin{pmatrix} l_i & \lambda & l_j \\ 0 & 0 & 0 \end{pmatrix} \begin{pmatrix} l_i & \lambda & l_j \\ -m_i & \mu & m_j \end{pmatrix}. \quad (36)$$

The Wigner $3j$ symbols and the values of spherical harmonics are computed by calling GSL. As eq. (36) vanishes for $\lambda > l_i + l_j$ or $\lambda < |l_i - l_j|$ or $\mu \neq m_i - m_j$, the range of the multi-polar expansion can be determined immediately after N_l , N_m and m_0 are given. We set $N_\lambda = 2l_{\max} + 1$, $N_\mu = N_m$ such that the index $i_\mu = |\mu| = 0, 1 \dots N_m - 1$ and $i_\lambda = \lambda - |\mu| = 0, 1 \dots N_\lambda - 1$ can cover all related terms in the multi-polar expansion. It should be notified that the $3j$ functions in GSL are not reliable for large l (it starts to fail violently near 80), which currently limits the application of the multi-polar program to large expansions.

3.5. Initial state

QPC-TDSE provides two ways to generate the initial state for propagation or analysis. The first one is to load the coefficients c_{nlm} from files, which are typically results saved from previous runs. In this case, the data stored in file should be prepared in a proper layout, whose details can be found in the user guide. Another one is to solve the generalized eigenvalue problem

$$E S c = [\mathcal{T} + \mathcal{U}] c. \quad (37)$$

For $U(\mathbf{r}) = 0$ cases, matrices in eq. (37) are block diagonal in lm -space thus the eigenvalue problem is solved by calling the LAPACK routines. Users may use the index vector (I_n, l_l, I_m) to order the quantum numbers of the eigenstate(s) they want according to $m = I_m + m_0$, $l = |m| + l_l$, $n = l + 1 + I_n$. The low-lying bound states can be computed to machine accuracy using a moderate box size r_{\max} , while for high-lying Rydberg states, convergent results can only be obtained using large r_{\max} .

For $U(\mathbf{r}) \neq 0$ cases, the right-hand-side matrix of eq. (37) is no longer block diagonal and a sparse eigenvalue problem is specified by including all lm -spaces. A copy of $\mathcal{T} + \mathcal{U}$ and S in hermitian CSR3 format is prepared and parsed to the FEAST [23] subprograms integrated in MKL to solve this sparse problem parallelly, which could take considerable time and memory for larger expansions and limit the application of current program. Users may designate the energy range to order the eigenstate(s) they want. Namely, by (E_{\min}, E_{\max}, I) , the I -th state in the energy range $E_{\min} \leq E \leq E_{\max}$ is selected. Due to the notorious property of slow convergence of the one-center expansion eq. (13), the accuracy of obtained eigenstates is usually limited for small N_l and N_m and will be improved very slowly at larger N_l and N_m . However, as we will show, they are sufficient for a large variety of practical purposes.

3.6. Propagator

QPC-TDSE employs the Crank-Nicolson method [24] together with the split operator technique [25] to solve eq. (18). There exist three types of Crank-Nicolson propagators in the current code.

The atomic Hamiltonian for $U(\mathbf{r}) = 0$ is propagated with similar procedures to ref. [8]. We have

$$\mathcal{U}^a(\tau) = \frac{S - \frac{i\tau}{2}\mathcal{T}}{S + \frac{i\tau}{2}\mathcal{T}} = \sum_{ml} \mathbf{1}_{ml} \otimes \frac{S - \frac{i\tau}{2}T^l}{S + \frac{i\tau}{2}T^l}, \quad (38)$$

where $(\mathbf{1}_{ml})_{m_l m_j, l_l l_j} = \delta_{m_l m_j} \delta_{l_l l_j}$. The propagation with eq. (38) is to apply the Crank-Nicolson kernel $(S + \frac{i\tau}{2}T^l)^{-1}(S - \frac{i\tau}{2}T^l)$ for $N_l N_m$ times. These kernels do not contain t , therefore the LU factorizations of the denominators $S + \frac{i\tau}{2}T^l$ are done before the propagation. There are $N_l N_m$ independent operations in the propagation of $\mathcal{U}^a(\tau)$, each having a complexity of $O(N_r)$, which are distributed to threads for parallelization. For $U(\mathbf{r}) \neq 0$, the propagator

$$\mathcal{U}^m(\tau) = \frac{S - \frac{i\tau}{2}(\mathcal{T} + \mathcal{U})}{S + \frac{i\tau}{2}(\mathcal{T} + \mathcal{U})} \quad (39)$$

does not exhibit simple structure without further split, therefore we treat its denominator by directly calling the parallel sparse linear solver PARDISO [26] provided in MKL. Similar to \mathcal{U}^a , the sparse LU factorization of $S + \frac{i\tau}{2}(\mathcal{T} + \mathcal{U})$ is done before propagation. The matrix-vector multiplication with $S - \frac{i\tau}{2}(\mathcal{T} + \mathcal{U})$ is composed of $N_l N_m$ independent groups of BLAS-like calls and is parallelized accordingly.

For the interaction part, further split is necessary to simplify its propagation. We adopt a slightly different method compared to ref. [8]. Consider the velocity gauge matrix $\mathcal{W}^s(t) = -A_s(t)\mathcal{D}^s - A_s(t)\mathcal{L}^s$ where

$$\mathcal{D}_{ij}^s = P_{m_l m_j, l_l l_j}^s D_{n_l n_j}, \quad (40)$$

$$\mathcal{L}_{ij}^s = Q_{m_l m_j, l_l l_j}^s L_{n_l n_j}. \quad (41)$$

We have

$$\begin{aligned} \mathcal{U}^z(\tau, t) &= \frac{S + \frac{i\tau}{2}A_z(t)\mathcal{D}^z}{S - \frac{i\tau}{2}A_z(t)\mathcal{D}^z} \times \frac{S + \frac{i\tau}{2}A_z(t)\mathcal{L}^z}{S - \frac{i\tau}{2}A_z(t)\mathcal{L}^z} \\ &= \left(\zeta^P \otimes I \right) \left(\sum_{lm} \mathbf{1}_{lm} \otimes \frac{S + \frac{i\tau}{2}Z_{lm}^P A_z(t)D}{S - \frac{i\tau}{2}Z_{lm}^P A_z(t)D} \right) \left(\zeta^{P\dagger} \otimes I \right) \\ &\quad \times \left(\zeta^Q \otimes I \right) \left(\sum_{lm} \mathbf{1}_{lm} \otimes \frac{S + \frac{i\tau}{2}Z_{lm}^Q A_z(t)L}{S - \frac{i\tau}{2}Z_{lm}^Q A_z(t)L} \right) \left(\zeta^{Q\dagger} \otimes I \right) \end{aligned} \quad (42)$$

where I is the N_r -by- N_r identity matrix, and the unitary matrices ζ^P, ζ^Q are the eigenvectors of the angular matrices P^z and Q^z with Z^P, Z^Q being their eigenvalue matrices such that

$$P^z = \zeta^P Z^P \zeta^{P\dagger}, \quad Q^z = \zeta^Q Z^Q \zeta^{Q\dagger}. \quad (43)$$

Also,

$$\begin{aligned} \mathcal{U}^x(\tau, t) &= \frac{S + \frac{i\tau}{4}A_x(t)(\mathcal{D}^+ + \mathcal{D}^-)}{S - \frac{i\tau}{4}A_x(t)(\mathcal{D}^+ + \mathcal{D}^-)} \times \frac{S + \frac{i\tau}{4}A_x(t)(\mathcal{L}^+ + \mathcal{L}^-)}{S - \frac{i\tau}{4}A_x(t)(\mathcal{L}^+ + \mathcal{L}^-)} \\ &= \left(\chi^P \otimes I \right) \left(\sum_{lm} \mathbf{1}_{lm} \otimes \frac{S + \frac{i\tau}{4}X_{lm}^P A_x(t)D}{S - \frac{i\tau}{4}X_{lm}^P A_x(t)D} \right) \left(\chi^{P\dagger} \otimes I \right) \\ &\quad \times \left(\chi^Q \otimes I \right) \left(\sum_{lm} \mathbf{1}_{lm} \otimes \frac{S + \frac{i\tau}{4}X_{lm}^Q A_x(t)L}{S - \frac{i\tau}{4}X_{lm}^Q A_x(t)L} \right) \left(\chi^{Q\dagger} \otimes I \right) \end{aligned} \quad (44)$$

$$\begin{aligned} \mathcal{U}^y(\tau, t) &= \frac{S - \frac{i\tau}{4}A_y(t)(\mathcal{D}^+ - \mathcal{D}^-)}{S + \frac{i\tau}{4}A_y(t)(\mathcal{D}^+ - \mathcal{D}^-)} \times \frac{S - \frac{i\tau}{4}A_y(t)(\mathcal{L}^+ - \mathcal{L}^-)}{S + \frac{i\tau}{4}A_y(t)(\mathcal{L}^+ - \mathcal{L}^-)} \\ &= \left(\nu^P \otimes I \right) \left(\sum_{lm} \mathbf{1}_{lm} \otimes \frac{S + \frac{i\tau}{4}Y_{lm}^P A_y(t)D}{S - \frac{i\tau}{4}Y_{lm}^P A_y(t)D} \right) \left(\nu^{P\dagger} \otimes I \right) \\ &\quad \times \left(\nu^Q \otimes I \right) \left(\sum_{lm} \mathbf{1}_{lm} \otimes \frac{S + \frac{i\tau}{4}Y_{lm}^Q A_y(t)L}{S - \frac{i\tau}{4}Y_{lm}^Q A_y(t)L} \right) \left(\nu^{Q\dagger} \otimes I \right) \end{aligned} \quad (45)$$

and

$$\frac{1}{2}(P^+ + P^-) = \chi^P X^P \chi^{P\dagger}, \quad \frac{1}{2}(Q^+ + Q^-) = \chi^Q X^Q \chi^{Q\dagger}, \quad (46)$$

$$\frac{i}{2}(P^+ - P^-) = \nu^P Y^P \nu^{P\dagger}, \quad \frac{i}{2}(Q^+ - Q^-) = \nu^Q Y^Q \nu^{Q\dagger}. \quad (47)$$

The diagonalization procedures of eqs. (43), (46), (47) is done by LAPACK before propagation. Propagation with eqs. (42), (44), (45) has been reduced into an interleaved combination of two species of operations: (1) performing forward/backward unitary transform in lm -space using ζ , χ and ν ; (2) propagating inside each lm -block by the Crank-Nicolson kernels in the form $(S - aD)^{-1}(S + aD)$ with the constant a computed from the products of A_x , A_y , A_z and eigenvalues given in X , Y , Z . To improve the performance, two neighboring unitary transforms are merged into one, and the partition structures of ζ , χ and ν are carefully taken into account. The unitary transforms are performed by calling the BLAS library embedded in MKL, which are internally parallelized. The propagation of odd or even space driven by elliptically polarized lasers as shown in Fig. 1 can be selectively skipped to further reduce the computational cost to about one quarter if the initial state falls in either space. The Crank-Nicolson kernels of eqs. (42), (44), (45) are parallelized in the same manner to eq. (38), except that the band LU factorization should be done at every time step, which occupies most of the execution time for relatively small expansions.

The propagation in length gauge is quite similar. From eq. (23), $\mathcal{W}^s(t) = E_s(t)\mathcal{R}^s$, thus the counterparts of eqs. (42), (44), (45) in length gauge are

$$\begin{aligned} \mathcal{U}^z(\tau, t) &= \frac{S - \frac{i\tau}{2}E_z(t)\mathcal{R}^z}{S + \frac{i\tau}{2}E_z(t)\mathcal{R}^z} \\ &= \left(\zeta^P \otimes I\right) \left(\sum_{lm} \mathbf{1}_{lm} \otimes \frac{S - \frac{i\tau}{2}Z_{lm}^P E_z(t)R}{S + \frac{i\tau}{2}Z_{lm}^P E_z(t)R}\right) \left(\zeta^{P\dagger} \otimes I\right), \end{aligned} \quad (48)$$

$$\begin{aligned} \mathcal{U}^x(\tau, t) &= \frac{S - \frac{i\tau}{4}E_x(t)(\mathcal{R}^+ + \mathcal{R}^-)}{S + \frac{i\tau}{4}E_x(t)(\mathcal{R}^+ + \mathcal{R}^-)} \\ &= \left(\chi^P \otimes I\right) \left(\sum_{lm} \mathbf{1}_{lm} \otimes \frac{S - \frac{i\tau}{4}X_{lm}^P E_x(t)R}{S + \frac{i\tau}{4}X_{lm}^P E_x(t)R}\right) \left(\chi^{P\dagger} \otimes I\right), \end{aligned} \quad (49)$$

$$\begin{aligned} \mathcal{U}^y(\tau, t) &= \frac{S + \frac{i\tau}{4}E_y(t)(\mathcal{R}^+ - \mathcal{R}^-)}{S - \frac{i\tau}{4}E_y(t)(\mathcal{R}^+ - \mathcal{R}^-)} \\ &= \left(\nu^P \otimes I\right) \left(\sum_{lm} \mathbf{1}_{lm} \otimes \frac{S - \frac{i\tau}{4}Y_{lm}^P E_y(t)R}{S + \frac{i\tau}{4}Y_{lm}^P E_y(t)R}\right) \left(\nu^{P\dagger} \otimes I\right). \end{aligned} \quad (50)$$

Finally, we may write down the total propagator for propagating $c_{nlm}(t_1)$ to $c_{nlm}(t_2)$ with $\Delta t = t_2 - t_1$:

$$\begin{aligned} c(t_2) &= \mathcal{U}^z\left(\frac{\Delta t}{2}, t_2\right) \mathcal{U}^y\left(\frac{\Delta t}{2}, t_2\right) \mathcal{U}^x\left(\frac{\Delta t}{2}, t_2\right) \\ &\quad \times \mathcal{U}^{a/m}(\Delta t) \\ &\quad \times \mathcal{U}^x\left(\frac{\Delta t}{2}, t_1\right) \mathcal{U}^y\left(\frac{\Delta t}{2}, t_1\right) \mathcal{U}^z\left(\frac{\Delta t}{2}, t_1\right) c(t_1). \end{aligned} \quad (51)$$

QPC-TDSE keeps a constant time step Δt throughout the propagation, although such constraint is not a requirement of the propagation algorithm. The local error of our propagation scheme at each time step is $O(\Delta t^3)$, originating from both the operator-splitting and the Padé's approximant used in Crank-Nicolson propagator. We have checked that the simulation results of this Crank-Nicolson propagator gradually coincide with that of another Lanczos-Arnoldi propagator as Δt becomes small. The code currently does not provide a built-in error analysis tool since the source of overall numerical error is very complicated and could vary from case to case, therefore results should always be carefully checked.

3.7. Absorber

To suppress the unphysical reflection near the box boundary, various methods have been developed. Multiplying mask functions [3], introducing a complex absorptive potential [8] and the irECS approach [27] are common choices.

QPC-TDSE applies a mask function onto the wavefunction after each propagation step, using

$$S c^{\text{masked}}(t) = \mathcal{M} c(t), \mathcal{M}_{ij} = \delta_{m_i m_j} \delta_{l_i l_j} M_{n_i n_j}. \quad (52)$$

The radial integral is just the matrix representation of the mask function $M(r)$:

$$M_{n_i n_j} = \int_{r_i}^{r_f} B_{n_i}(r) M(r) B_{n_j}(r) dr. \quad (53)$$

To perform eq. (52), the time-independent matrix M and the Cholesky factorization of S are prepared ahead of propagation. Absorption in each lm -subspace can be performed parallelly. In practice, we use

$$M(r) = \begin{cases} 1, & r \leq r_L \\ \cos^\alpha \left[\frac{\pi(r - r_L)}{2(r_H - r_L)} \right], & r_L < r \leq r_H. \end{cases} \quad (54)$$

r_L , r_H and α are user-given values.

3.8. Observable

QPC-TDSE supports the run-time evaluation of any dipolar observables in the form

$$O_z[f] = f(r) \cos(\theta), O_{\pm}[f] = f(r) \sin(\theta) \exp(\pm i\varphi), \quad (55)$$

where $f(r)$ is an arbitrary close-form functions. For dipole moment, users may set it to $f(r) = -r$. For dipole acceleration in $U(\mathbf{r}) = 0$ cases, users may set it according to the exact form of $-\nabla V_c$. The current code does not support the direct evaluation of dipole acceleration for $U(\mathbf{r}) \neq 0$ since it has a complicated form and alternative approaches exist. The observables of eq. (55) equal

$$\langle O_s \rangle(t) = \sum_{n_i l_i m_i, n_j l_j m_j} c_{n_i l_i m_i}^*(t) c_{n_j l_j m_j}(t) f_{n_i n_j} P_{m_i m_j, l_i l_j}^s \quad (56)$$

The radial integral

$$f_{n_i n_j} = \int_{r_i}^{r_f} B_{n_i}(r) f(r) B_{n_j}(r) dr \quad (57)$$

is performed and stored in the same way to eqs. (24), (25), (26), (27), (28) before propagation.

3.9. Momentum spectra via projection onto continuum states

As illustrated by Fetić [15], if the exact scattering state is achievable, the projection onto continuum states (PCS) approach with B-spline basis is capable of providing high-fidelity PMD for atomic model potentials, which could serve as a benchmark for other methods.

QPC-TDSE provides PCS approach for $U(\mathbf{r}) = 0$ cases. It is optionally performed at the end of the propagation for requested asymptotic momentum $\mathbf{k} = (k, \theta_k, \varphi_k)$. Although the exact form of scattering state for $U(\mathbf{r}) \neq 0$ is known for some special systems [28] and for the general one-electron problem it can be computed precisely via methods based on the multi-channel scattering theory [29], their PCS have not yet been implemented in QPC-TDSE. Following ref. [15], the code first evaluates the partial wave projection

$$P_{lm}(k) = \sqrt{\frac{2}{\pi}} \sum_n c_{nlm}(t_f) I_{lm}(k), \quad (58)$$

where

$$I_{lm}(k) = k^{-1} \int_{r_i}^{r_f} w_l(kr) B_n(r) dr. \quad (59)$$

Here $w_l(kr)$ is the regular solution to

$$\frac{d^2 w}{d\rho^2} + \left\{ 1 - \frac{l(l+1)}{\rho^2} - \frac{2V_c(\rho/k)}{k^2} \right\} w = 0. \quad (60)$$

For pure Coulomb potential $V_c(r) = -Z/r$, eq. (60) is the well-known Coulomb wave equation with the Sommerfeld parameter $\eta = -Z/k$. Its solution(s), the Coulomb wave function(s) together with the Coulomb phase shift $\sigma_l(k)$ are thus evaluated with extended precision by a code adapted from the COULOMBFG recipe [30]. For other cases, it is solved by a fourth-order Runge-Kutta solver starting from $kr = \epsilon_1 > 0$, with the general initial condition obtained from a Taylor expansion truncated at the first order

$$w_l(\epsilon_1) = \epsilon_2, w'_l(\epsilon_1) = \epsilon_2 \times \frac{(l+1)}{\epsilon_1} \quad (61)$$

Here $\epsilon_{1,2}$ are small numbers and we have assumed near singularity

$$\lim_{r \rightarrow 0} r^2 V_c(r) = 0. \quad (62)$$

Also assumed are

$$\lim_{r \rightarrow \infty} r V_c(r) = Z, \lim_{r \rightarrow \infty} V_c(r) = 0, \quad (63)$$

such that the phase shift $\Delta_l(k) = \sigma_l(k) + \delta_l(k)$ and the correct normalization are determined by matching the solution to the Coulomb wave in asymptotic region:

$$\frac{w'_l}{w_l} = \frac{\exp(+i\delta_l) H_{l,\eta}^{\prime+} - \exp(-i\delta_l) H_{l,\eta}^{\prime-}}{\exp(+i\delta_l) H_{l,\eta}^{\prime+} - \exp(-i\delta_l) H_{l,\eta}^{\prime-}}. \quad (64)$$

The solver's tolerance of absolute error and relative error is inlined in the code as 5×10^{-11} .

Note that the above assumptions are restrictions for applying PCS approach only. The propagation scheme works for arbitrary well-behaved $V_c(r)$, even if they are not subject to these restrictions, for example $V_c(r) = r^2$. These restrictions merely limit the application of the programme because most single-electron models in atomic ionization problems fall in these forms.

Users may then choose to output $P_{lm}(k)$ to conduct partial wave analysis or to obtain the photo-electron energy spectra by summing them up:

$$PES(E) = \sqrt{2E} \sum_{lm} |P_{lm}(\sqrt{2E})|^2. \quad (65)$$

For PMD, the code will evaluate next

$$PMD(\mathbf{k}) = \left| \sum_{lm} (-i)^l \exp(i\Delta_l(k)) Y_l^m(\theta_k, \varphi_k) P_{lm}(k) \right|^2. \quad (66)$$

For reusing intermediate quantities, the requested \mathbf{k} are assumed to be on a mesh spanned by $\{k_s\}_{s=0}^{N_k-1}$, $\{\theta_{ks}\}_{s=0}^{N_{\theta_k}-1}$ and $\{\varphi_{ks}\}_{s=0}^{N_{\varphi_k}-1}$. For other types of grids, interpolations are necessary.

Since Eq. (6) are not restrictive to $U(\mathbf{r}) = 0$ cases and we implemented it using the same code, by setting $\Delta_l(\mathbf{k}) = 0$ and [31]

$$I_{ln}(k, r_0) = \int_{r_i}^{r_f} r j_l(kr) \Theta(r - r_0) B_n(r) dr. \quad (67)$$

Here j_l are spherical Bessel functions of the first kind. They are also evaluated by the COULOMBFG recipe.

The most time-consuming stage of PCS is the solution of w_l at various k and r , whose temporal complexity scales with $O(l_{\max} N_k N_r)$ and is parallelized to boost its evaluation. Besides, the intervals between $\{k_s\}$ should be sparse enough compared to the density of states in the spherical box, otherwise unphysical oscillations may occur in the calculated spectrum. The latter can be estimated by π/r_{\max} .

3.10. Momentum spectra via time-dependent surface flux

QPC-TDSE implements eq. (7) by the following integral rule:

$$PMD(\mathbf{k}) = \sqrt{\frac{2}{\pi}} \Delta t \sum_j a_{\mathbf{k}}(t_j) \exp(i\Phi_{\mathbf{k}}(t_j)) + O(\Delta t^2), \quad (68)$$

where we have assumed that $a_{\mathbf{k}}(t_0) = a_{\mathbf{k}}(t_f) = 0$. Here the Volkov phase compatible with eq. (8) is

$$\Phi_{\mathbf{k}}(t) = \int_{-\infty}^t \left(\frac{\mathbf{k}^2}{2} + \mathbf{A}(\tau) \cdot \mathbf{k} \right) d\tau, \quad (69)$$

and the surface amplitude is

$$a_{\mathbf{k}}(t) = \sum_{lm} (-i)^{l+1} Y_l^m(\Omega_k) a_{klm}(t). \quad (70)$$

The incomplete partial wave surface amplitude on the right-hand side is

$$a_{klm}(t) = -\frac{1}{2} \sum_n c_{nlm}(t) \left\{ r j_l(kr) \overleftrightarrow{\partial_r} B_n(r) \right\}_{r=r_0} - i \sum_{l'm'} \left\{ A_z(t) P_{mm',ll'}^z + \frac{A_+(t)}{2} P_{mm',ll'}^+ + \frac{A_-(t)}{2} P_{mm',ll'}^- \right\} \sum_n c_{nl'm'}(t) \left\{ r j_l(kr) B_n(r) \right\}_{r=r_0}, \quad (71)$$

which is numerically summed up during propagation. A complete partial wave surface amplitude [32] which accounts for the angular dependency of eq. (69) has not yet been implemented in this code though.

Similar to PCS, for reusing intermediate values, requested \mathbf{k} points follow the same scheme as mentioned before. It should be notified that if the integral eq. (7) is truncated at t_f , the wavepackets residing in the region $|\mathbf{r}| < r_0$ will not be accounted for, which affects the convergency of low energy part in the spectrum. The formal patch to solve this problem, the i-SURF [19] approach, has not yet been implemented in QPC-TDSE. Users may elongate the simulation time by setting the free-propagation parameter $t_d \approx r_0/k_{\min}$ to overcome this problem, where k_{\min} is the lowest interested value of the electron's momentum. Besides, it is recommended to remove the long Coulomb tail when using t-SURFF since it could cause unphysical structures in the low energy region of the spectrum [33].

4. Examples

Examples are provided to illustrate the capability of the program to solve problems of interest. To run any examples in this section within one command, one may launch the bash scripts in the directory named *script*. Each script will compile a binary with a preset config file which contains a list of parameters and settings (e.g., workflow control flags, grid parameters etc.) and then run it with proper arguments. The exact meanings of these parameters and the procedures to conduct a customized simulation are presented in the user guide in detail. The computational resources consumed by these examples are dominated by the scale of the simulation, which is directly determined by the grid and laser parameters. They are listed in Table 1 for clarity. The plotting scripts written in Matlab language could be found in the directory *analysis*.

Table 1
Parameters and performances in examples.

Example name	N_r	N_l	N_m	m_0	$N_{threads}$	r_{max}	N_t	Time ^{a,b}
01-a-gs	5000	1	1	0	1	2400	N/A	3 m 36 s
01-a	5000	40	1	0	10	2400	16535	6 m 10 s
01-b	640	40	1	0	10	310	66535	5 m 58 s
01-c-gs	5000	1	1	0	1	2400	N/A	3 m 32 s
01-c	5000	160	1	0	40	2400	66139	83 m 07 s
02-a	500	8	26	-20	8	240	2756	0 m 49 s
02-b	400	18	150	-11	40	200	66139	184 m 46 s
03-a-gs	300	40	1	0	10	144	N/A	0 m 24 s ^b
03-a	300	40	1	0	10	144	176371	88 m 40 s ^b

^a The typical total wall-clock time of an exclusive run of the example script for reference, which was measured on a server with two NUMA nodes, each installed with an E6248. Threads were distributed across nodes by default since we did not explicitly bind threads to cores.

^b A full execution of the scripts contains multiple TDSE runs.

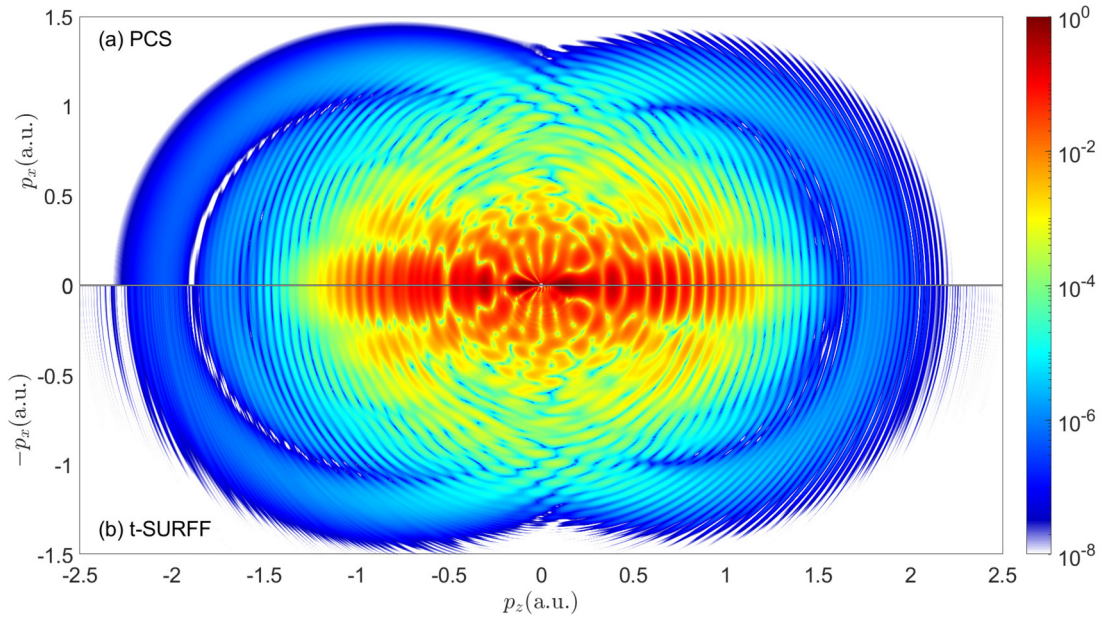


Fig. 2. Photo-electron momentum distribution in $p_y = 0$ plane of an hydrogen atom exposed to a \sin^2 linearly polarized laser with $\omega = 0.057$, $N_c = 6$ and $A_{0z} = 0.9364$, computed via (a) PCS (b) t-SURFF. The spectrum is normalized in momentum.

4.1. Atomic above threshold ionization

As one of the fundamental laser-driven processes, above threshold ionization (ATI) has been studied intensively in the literature and can serve as good examples for illustration. Explanation of the fine structures in the spectrum is beyond the purpose of this article and we will only concentrate on the computational aspects.

The first example aims at the accurate computation of ATI spectra of hydrogen atom under a linearly polarized 6-cycle 800 nm laser with a \sin^2 envelope for comparison with ref. [15]. The laser field is expressed as

$$A_z(t) = A_{0z} \sin(\omega t) \sin^2\left(\frac{\pi t}{2N_c}\right). \quad (72)$$

The results shown in Fig. 2(a) and (b) are computed via immediately performing PCS at the instant that the laser is off and via t-SURFF with a total free propagation time of 2000 a.u., respectively. The t-SURFF boundary is at $r_0 = 200$. The laser intensity is 1×10^{14} W/cm². For linearly polarized lasers, it is sufficient to show only the $p_y = 0$ plane, and the results given by the two methods agree well on the overall structure of spectrum except that near $|\mathbf{k}| < 0.3$ unphysical oscillatory structures start to occur for t-SURFF, which could be suppressed by either longer free propagation time or better boundary absorbers. Besides, a relatively poorer noise level is found for t-SURFF under the current simulation parameters, although it merely influences the principal structure of the spectrum. To reproduce these results, one may run the scripts **example01-a-gs**, **example01-a** and **example01-b** sequentially.

We demonstrate the use of non-hydrogenic potentials with a more resource-demanding example, i.e. the ATI spectra of helium atom characterized by a model potential [34]. The laser parameters in this example are the same to the previous ones except that the intensity is turned up to 4×10^{14} W/cm² such that the electron may tunnel through the deeper barrier ($I_p \approx 0.9038$), and the wavefunction is accordingly expanded to $l_{max} \approx (I_p + 10.07U_p)/\omega \approx 160$ and $r_{max} \approx 2.24A_{0z} \times 2\pi N_c/\omega \approx 2400$ to hold the full ionized wavepacket such that the application of the projection method is possible. To obtain converged results for such a stronger laser, the time step is also set smaller to 0.01. The spectrum computed via PCS is shown in Fig. 3. One may reproduce it by the script **example01-c-gs** and **example01-c**. We shall notify that in the current implementation of the radial Runge-Kutta solver, upflow and loss of precision could occur near the

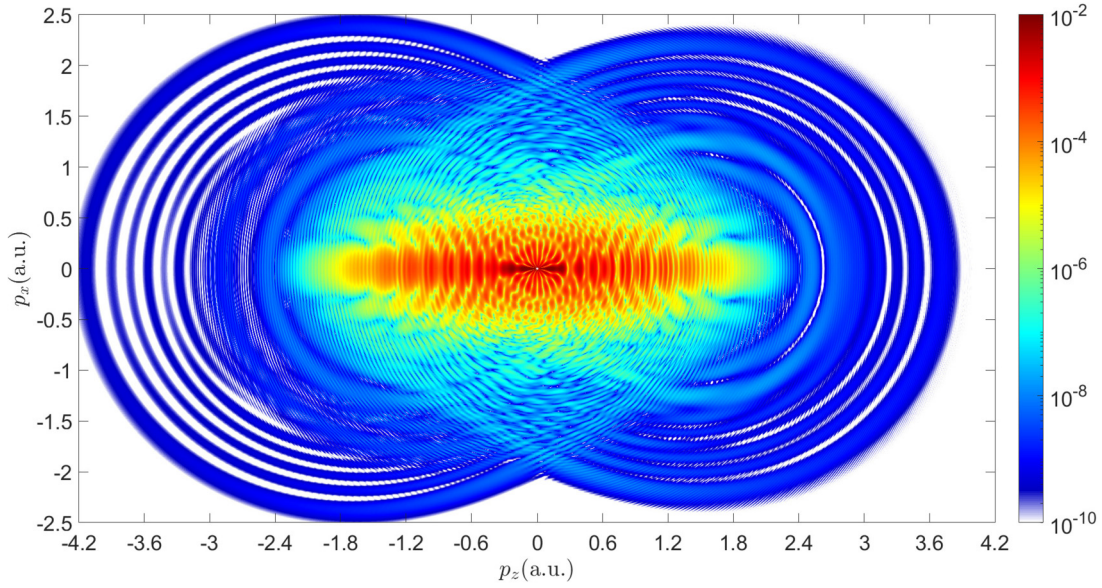


Fig. 3. Photo-electron momentum distribution in $p_y = 0$ plane of a model helium atom exposed to a \sin^2 linearly polarized laser with $\omega = 0.057$, $N_c = 6$ and $A_{0z} = 1.8728$. The spectrum is normalized in momentum.

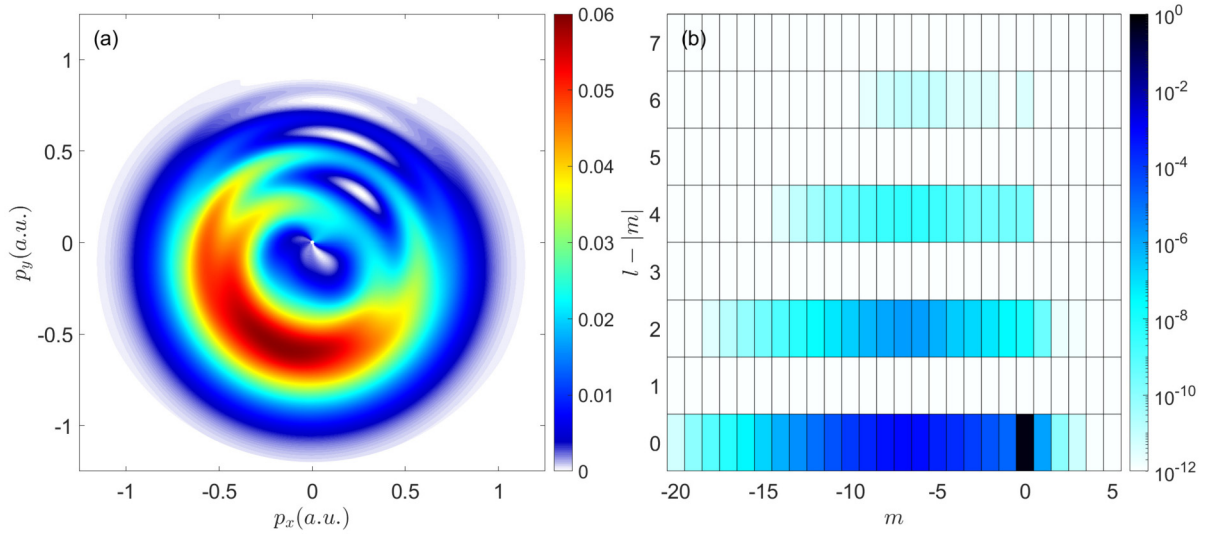


Fig. 4. (a) Photo-electron momentum distribution in $p_z = 0$ plane of a hydrogen atom exposed to a \sin^2 circularly polarized laser with $\omega = 0.114$, $N_c = 2$ and $A_{0x} = A_{0y} = 0.4682$. The spectra are normalized in energy. (b) The maximal values of the norm of expansion coefficients, namely $|c_{lm}(t_f)|^2$, for each (l, m) . Subspaces with odd-valued $l - |m|$ are never populated due to the selection rule.

origin for extremely large l and the results should be carefully checked. The exact value of l for such instability to occur depends on the potential model.

4.2. Attosecond clock

As a verification of the current program, we reproduce the example given in ref. [33] where a 2-cycle 400 nm circularly polarized laser with a \sin^2 envelope is used to ionize the hydrogen atom. The corresponding script is named with **example02-a**. At this time, the projection method is used instead of t-SURFF to remove the artifacts in low-energy region, as shown in Fig. 4(a). Note that the laser fields in this section are expressed by

$$A_x(t) = A_{0x} \sin(\omega t) \sin^n\left(\frac{\omega t}{2N_c}\right), A_y(t) = A_{0y} \cos(\omega t) \sin^n\left(\frac{\omega t}{2N_c}\right). \quad (73)$$

A course estimation according to $\mathbf{p} \approx -\mathbf{A}$ for ionized electron suggests that the wavepacket could reach $m = (I_p + A_0^2/2)/\omega \approx 6$ on average, while in practice the expansion should include about two or three times of it to reach convergency. As indicated by Fig. 5(b), the advantage of adopting the current grid-scheme in the simulation for ellipticity near 1 is evident, where the major part of the ionized wavepacket travels near $l - |m| = 0$. In the current scheme, only $N_l N_m = 208$ spherical harmonics are sufficient to hold the full wavepackets, compared to that of $(l_{\max} + 1)^2 = 441$ for a full expansion up to $l_{\max} = 20$.

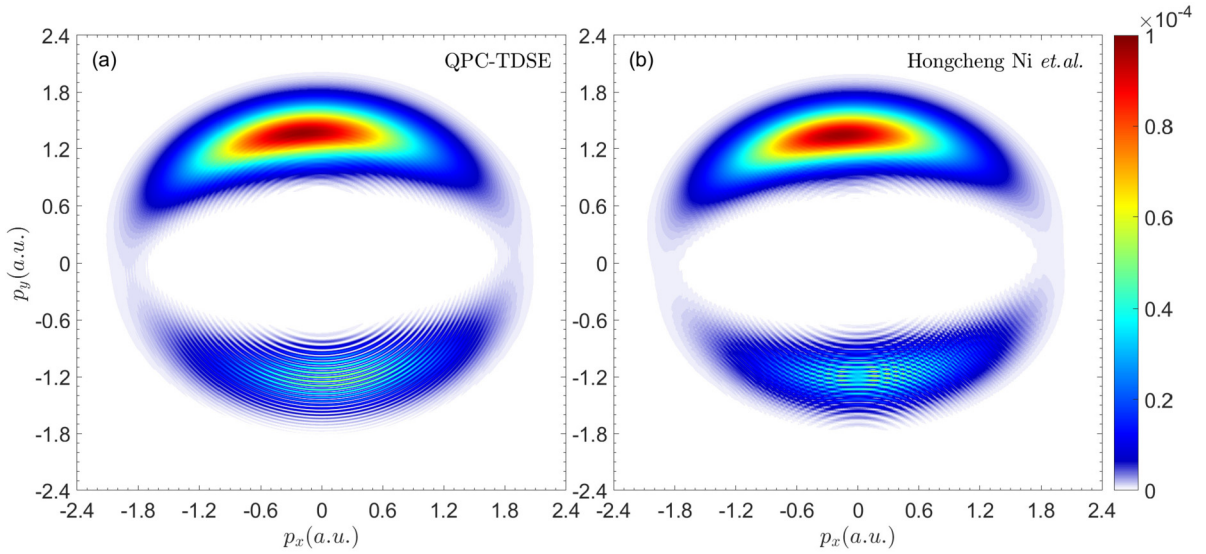


Fig. 5. Photo-electron momentum distribution in $p_z = 0$ plane of a helium atom exposed to a \sin^4 elliptically polarized laser with $\omega = 0.57$, $N_c = 6$ and $A_{0x} = 1.1651$ and $A_{0y} = -1.2563$, given (a) by QPC-TDSE (b) by ref [35] (data for the plot are from personal communications). The spectrum is normalized in energy.

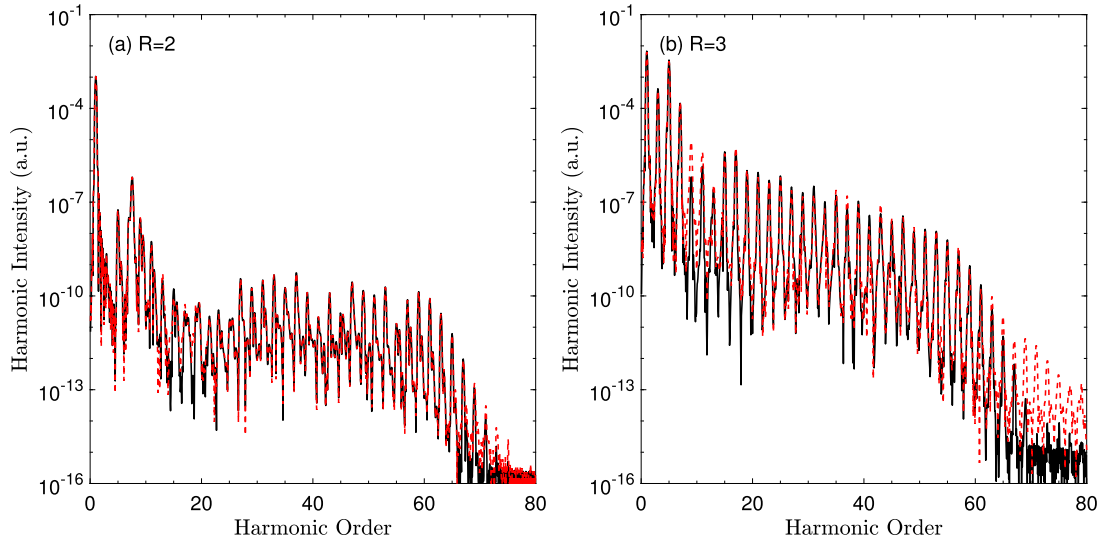


Fig. 6. The power spectra of the high harmonic generation from a H_2^+ whose internuclear distance is fixed at (a) $R = 2$ (b) $R = 3$. The black solid lines are given by the current QPC-TDSE code, and the red dotted lines are given by another Lanczos-Arnoldi TDSE solver which expands the wavefunction in prolate spheroidal coordinates.

Such advantage is more prominent for the stronger laser in **example02-b**. As a working example in the study the subcycle momentum transfer in strong-field tunneling ionization [35], a model helium atom is ionized by a 6-cycle \sin^4 laser whose intensity is $5 \times 10^{14} \text{ W/cm}^2$ and ellipticity is 0.75. Although the current code does not include the non-dipole effects, it is still valid to compare the momentum distribution in the $p_z = 0$ plane since their differences are of $1/c^2$ order. The spectrum shown in Fig. 5(a)(b) are in good agreement. A course estimate suggests that the ionized wavepacket could reach $m = 55$ on average, while in practice the maximal value of m is set to 138 to get accurate PMD via t-SURFF. The number of involved partial waves in this example is about 14% of that in a full expansion until $l = 138$, which significantly saves computational resources. However, we shall note that this expansion scheme does not exhibit evident advantages when there exist transitions to larger $l - |m|$, which could happen, for example, when the electron is driven by a laser linearly polarized in x direction or an orthogonal two-color laser.

4.3. High harmonic generation

Molecular high harmonic generation is known to exhibit abundant fine structures on the spectra and are sensitive to the orientation angles and nuclear distance [36]. To illustrate the use of multi-polar potential as well as the computation of harmonic generation spectrum, we provide **example03-a-gs** and **example03-a**. Despite the fact that the ground state energy computed at $N_l = 40$ is only accurate to four digits due to the slow convergency of OCE, the high harmonic spectrum of fixed-nuclei H_2^+ at different internuclear distances as shown in Fig. 6(a) and (b) still satisfactorily match with the results given by another spheroidal TDSE solver. The driving laser in this example is a $3 \times 10^{14} \text{ W/cm}^2$ 800 nm laser polarized in the same direction to the molecular axis and has a trapezoidal envelope with 2-cycle ramps on both sides and a 12-cycle platform in the middle. The significant difference in the magnitude of harmonic intensity between the $R = 2$ and $R = 3$ cases could be attribute to the sensitive dependency of ionization rate upon the internuclear distance [37].

Due to the limit of computational resources for the sparse linear system algorithms adopted in the propagator, the program with static multi-polar potentials has not been successfully applied to large N_m expansions yet, which is required by any long wavelength lasers polarized in different directions to the axis of the linear molecule, or by the more general and complicated non-linear molecules. Nevertheless, the non-parallel few-photon ionization of linear molecules which requires a limited N_m is still possible and will not be discussed here.

5. Conclusion

In conclusion, we present a new code for solving the TDSE of laser-driven atoms and molecules within the single-active-electron and dipole approximations. It improves some of the methods in the existing TDSE packages and adds new features for the efficient and accurate evaluation of concerned physical quantities. The successful applications to the above-discussed scenarios have shed light on its potential prospects on these topics. The less satisfactory quadratic scaling behavior of the propagation algorithm with respect to the number of partial waves does not significantly limits its use within a wide range of situations.

CRediT authorship contribution statement

Zhao-Han Zhang: Conceptualization, Formal analysis, Methodology, Project administration, Software, Writing – original draft, Writing – review & editing. **Yang Li:** Funding acquisition, Validation. **Yi-Jia Mao:** Software, Validation. **Feng He:** Funding acquisition, Supervision, Writing – review & editing.

Declaration of competing interest

The authors declare that they have no known competing financial interests or personal relationships that could have appeared to influence the work reported in this paper.

Data availability

Data will be made available on request.

Acknowledgements

This work was supported by National Natural Science Foundation of China (Grants Nos. 12274294, 11925405 and 91850203), National Key R&D Program of China (2018YFA0404802).

Appendix A. Supplementary material

Supplementary material related to this article can be found online at <https://doi.org/10.1016/j.cpc.2023.108787>.

References

- [1] F. Krausz, M. Ivanov, *Rev. Mod. Phys.* 81 (1) (2009) 163–234, <https://doi.org/10.1103/RevModPhys.81.163>.
- [2] Y. Huisman, A. Rouzée, A. Gijbels, J. Jungmann, A. Smolkowska, P. Logman, F. Lepine, C. Cauchy, S. Zamith, T. Marchenko, et al., *Science* 331 (6013) (2011) 61–64, <https://doi.org/10.1126/science.1198450>.
- [3] J.L. Krause, K.J. Schafer, K.C. Kulander, *Phys. Rev. Lett.* 68 (24) (1992) 3535–3538, <https://doi.org/10.1103/PhysRevLett.68.3535>.
- [4] H. Wang, M. Chini, S. Chen, C.-H. Zhang, F. He, Y. Cheng, Y. Wu, U. Thumm, Z. Chang, *Phys. Rev. Lett.* 105 (2010) 143002, <https://doi.org/10.1103/PhysRevLett.105.143002>.
- [5] J. Zhu, A. Scrinzi, *Phys. Rev. A* 101 (6) (2020) 063407, <https://doi.org/10.1103/PhysRevA.101.063407>.
- [6] A.U. Lode, C. Lévesque, L.B. Madsen, A.I. Streltsov, O.E. Alon, *Rev. Mod. Phys.* 92 (1) (2020) 011001, <https://doi.org/10.1103/RevModPhys.92.011001>.
- [7] M.A. Marques, A. Castro, G.F. Bertsch, A. Rubio, *Comput. Phys. Commun.* 151 (1) (2003) 60–78, [https://doi.org/10.1016/S0010-4655\(02\)00686-0](https://doi.org/10.1016/S0010-4655(02)00686-0).
- [8] D. Bauer, P. Koval, *Comput. Phys. Commun.* 174 (5) (2006) 396–421, <https://doi.org/10.1016/j.cpc.2005.11.001>.
- [9] C.Ó. Broin, L. Nikolopoulos, *Comput. Phys. Commun.* 185 (6) (2014) 1791–1807, <https://doi.org/10.1016/j.cpc.2014.02.019>.
- [10] S. Patchkovskii, H. Muller, *Comput. Phys. Commun.* 199 (2016) 153–169, <https://doi.org/10.1016/j.cpc.2015.10.014>.
- [11] X. Guan, C.J. Noble, O. Zatsarinny, K. Bartschat, B.I. Schneider, *Comput. Phys. Commun.* 180 (12) (2009) 2401–2409, <https://doi.org/10.1016/j.cpc.2009.03.005>.
- [12] Y. Fu, J. Zeng, J. Yuan, *Comput. Phys. Commun.* 210 (2017) 181–192, <https://doi.org/10.1016/j.cpc.2016.09.016>.
- [13] H. Bachau, E. Cormier, P. Decleva, J. Hansen, F. Martín, *Rep. Prog. Phys.* 64 (12) (2001) 1815, <https://doi.org/10.1088/0034-4885/64/12/205>.
- [14] L. Madsen, L. Nikolopoulos, T. Kjeldsen, J. Fernández, *Phys. Rev. A* 76 (6) (2007) 063407, <https://doi.org/10.1103/PhysRevA.76.063407>.
- [15] B. Fetić, W. Becker, D. Milošević, *Phys. Rev. A* 102 (2) (2020) 023101, <https://doi.org/10.1103/PhysRevA.102.023101>.
- [16] L. Tao, A. Scrinzi, *New J. Phys.* 14 (1) (2012) 013021, <https://doi.org/10.1088/1367-2630/14/1/013021>.
- [17] A.D. Bandrauk, F. Fillion-Gourdeau, E. Lorin, *J. Phys. B, At. Mol. Opt. Phys.* 46 (15) (2013) 153001, <https://doi.org/10.1088/0953-4075/46/15/153001>.
- [18] E. Cormier, P. Lambropoulos, *J. Phys. B, At. Mol. Opt. Phys.* 29 (9) (1996) 1667, <https://doi.org/10.1088/0953-4075/29/9/013>.
- [19] F. Morales, T. Bredtmann, S. Patchkovskii, *J. Phys. B, At. Mol. Opt. Phys.* 49 (24) (2016) 245001, <https://doi.org/10.1088/0953-4075/49/24/245001>.
- [20] J.C. Baggesen, L.B. Madsen, *J. Phys. B, At. Mol. Opt. Phys.* 44 (11) (2011) 115601, <https://doi.org/10.1088/0953-4075/44/11/115601>.
- [21] M. Wu, S. Chen, S. Camp, K.J. Schafer, M.B. Gaarde, *J. Phys. B, At. Mol. Opt. Phys.* 49 (6) (2016) 062003, <https://doi.org/10.1088/0953-4075/49/6/062003>.
- [22] H.-B. Yao, Q.-W. Qu, Z.-H. Zhang, J.-W. Wang, J. Gao, C.-X. Hu, H. Li, J. Wu, F. He, *Phys. Rev. Lett.* 130 (2023) 113201, <https://doi.org/10.1103/PhysRevLett.130.113201>.
- [23] E. Polizzi, *Phys. Rev. B* 79 (11) (2009) 115112, <https://doi.org/10.1103/PhysRevB.79.115112>.
- [24] J. Crank, P. Nicolson, in: *Math. Proc. Camb. Philos. Soc.*, vol. 43, Cambridge University Press, 1947, pp. 50–67.
- [25] M.R. Hermann, J. Fleck Jr., *Phys. Rev. A* 38 (12) (1988) 6000–6012, <https://doi.org/10.1103/PhysRevA.38.6000>.
- [26] O. Schenk, K. Gärtner, W. Fichtner, A. Stricker, *Future Gener. Comput. Syst.* 18 (1) (2001) 69–78, [https://doi.org/10.1016/S0167-739X\(00\)00076-5](https://doi.org/10.1016/S0167-739X(00)00076-5).
- [27] A. Scrinzi, *Phys. Rev. A* 81 (5) (2010) 053845, <https://doi.org/10.1103/PhysRevA.81.053845>.
- [28] E.W. Leaver, *J. Math. Phys.* 27 (5) (1986) 1238–1265, <https://doi.org/10.1063/1.527130>.
- [29] A. Palacios, J.L. Sanz-Vicario, F. Martín, *J. Phys. B, At. Mol. Opt. Phys.* 48 (24) (2015) 242001, <https://doi.org/10.1088/0953-4075/48/24/242001>.
- [30] I.J. Thompson, A.R. Barnett, *J. Comput. Phys.* 64 (2) (1986) 490–509, [https://doi.org/10.1016/0021-9991\(86\)90046-X](https://doi.org/10.1016/0021-9991(86)90046-X).
- [31] B. Fetić, M. Tunja, W. Becker, D. Milošević, *Phys. Rev. A* 105 (5) (2022) 053121, <https://doi.org/10.1103/PhysRevA.105.053121>.

- [32] V. Mosert, D. Bauer, Comput. Phys. Commun. 207 (2016) 452–463, <https://doi.org/10.1016/j.cpc.2016.06.015>.
- [33] V. Tulsy, D. Bauer, Comput. Phys. Commun. 251 (2020) 107098, <https://doi.org/10.1016/j.cpc.2019.107098>.
- [34] X. Tong, C. Lin, J. Phys. B, At. Mol. Opt. Phys. 38 (15) (2005) 2593, <https://doi.org/10.1088/0953-4075/38/15/001>.
- [35] H. Ni, S. Brennecke, X. Gao, P.-L. He, S. Donsa, I. Březinová, F. He, J. Wu, M. Lein, X.-M. Tong, J. Burgdörfer, Phys. Rev. Lett. 125 (2020) 073202, <https://doi.org/10.1103/PhysRevLett.125.073202>.
- [36] M. Lein, N. Hay, R. Velotta, J.P. Marangos, P. Knight, Phys. Rev. Lett. 88 (18) (2002) 183903, <https://doi.org/10.1103/PhysRevLett.88.183903>.
- [37] T. Zuo, A.D. Bandrauk, Phys. Rev. A 52 (4) (1995) R2511–R2514, <https://doi.org/10.1103/PhysRevA.52.R2511>.